Enhancing alkaline water oxidation with NiFe alloy-encapsulated nitrogen-doped vertical graphene array

Jue Nan[1], Beirong Ye[2], Xun He[2], Chen Li[2], Wanli Zhang[1], Qian Liu[3], Luming Li[3], Wei Chu[3], Xuping Sun[2,4] (✉), and Yongqi Zhang[2] (✉)

[1] School of Integrated Circuit Science and Engineering, University of Electronic Science and Technology of China, Chengdu 611731, China
[2] Institute of Fundamental and Frontier Science, University of Electronic Science and Technology of China, Chengdu 611731, China
[3] Institute for Advanced Study, Chengdu University, Chengdu 610106, China
[4] College of Chemistry, Chemical Engineering and Materials Science, Shandong Normal University, Jinan 250014, China

ABSTRACT

Advancing efficient and affordable electrocatalysts to boost the oxygen evolution reaction (OER) is pivotal for sustainable green hydrogen production. Herein, we propose the fabrication of nickel-iron alloy nanoparticles-encapsulated on N-doped vertically aligned graphene array on carbon cloth (NiFe@NVG/CC) as a highly active three-dimensional (3D) catalyst electrode for OER. In 1 M KOH, such NiFe@NVG/CC demonstrates outstanding catalytic performance, necessitating merely overpotential of 245 mV for achieving a current density of 10 mA·cm^{-2}, a remarkably low Tafel slope of 36.2 mV·dec^{-1}. Furthermore, density functional theory calculations validate that the incorporate of N species into graphene can reinforce the electrocatalytic activity though reducing the reaction energy barrier during the conversion of *O to *OOH intermediates. The outstanding performance and structural benefits of NiFe@NVG/CC offer valuable insights for the development of innovative and efficient electrocatalysts for water oxidation.

1 Introduction

Hydrogen (H$_2$) is recognized as a clean and sustainable energy carrier, offering a viable alternative to fossil fuels and natural gases. Its notably high energy density and production of zero carbon emissions make it particularly attractive [1–3]. One effective method for producing H$_2$ is water electrolysis [4–10]. However, the process faces a significant challenge during the anodic oxygen evolution reaction (OER). This reaction, crucial for water electrolysis, involves a complex multi-electron transfer process to form covalent O–O bonds and is hindered by slow reaction kinetics [11–18]. To address this, active OER electrocatalysts are essential for reducing the substantial overpotential required. Unfortunately, the benchmarked OER electrocatalysts, RuO$_2$ and IrO$_2$, are limited by their low abundance and high cost, impeding their broader application.

Recently, 3d transition metals and their compounds have risen to prominence as viable substitutes for noble metals for their cost-effectiveness, abundant availability, and exceptional catalytic properties [19–26]. Nickel-iron (NiFe) bimetallic catalysts are particularly notable within this group for their synergistic effect, which contributes to low overpotential and increased durability, especially under alkaline conditions [22, 25, 27–30]. Nevertheless, bare NiFe catalysts that come into direct contact with liquid electrolytes are susceptible to erosion, and the particles within these catalysts can agglomerate during the water oxidation, leading to a significant decline in catalytic performance [27, 28]. Presently,

the integration of these catalysts with nano carbonaceous materials to create carbon-encapsulated composites has been conclusively demonstrated as an efficacious approach for enhancing their electrocatalytic performance [22, 31–35]. As an illustrative case, Zhang et al. showcased significant catalytic activity through the synthesis of nitrogen (N)-doped carbon-encapsulated NiFe nanoparticles via a one-step calcination process with a precursor derived from metal organic compounds. Notably, their catalytic activity demonstrated superior performance compared to RuO$_2$ for OER [34]. The research team, led by Han, reported their work on encapsulating NiFe alloy nanoparticles in carbon nanofibers, which resulted in highly efficient water oxidation [22]. While innovative carbon-encapsulated NiFe nanomaterials have demonstrated improved catalytic performance for the protective carbon shell and enhanced conductivity, challenges arise from excessively thick carbon layers and limited specific surface areas in electrocatalysts for exposing more active sites. Also, the necessity for binders has proven detrimental to the catalytic performance of NiFe for OER. Three-dimensional (3D) vertically aligned graphene (VG) nanosheet array, with its open channels, abundant edges, large specific surface areas, and excellent conductivity, is considered the ideal 3D scaffold for active materials and has been widely used in the realm of electrochemical energy storage and conversion [36–39]. It is envisaged that 3D VG array encapsulating NiFe will serve as an ideal OER electrocatalyst, a potential that remains to be explored.

Address correspondence to Xuping Sun, xpsun@uestc.edu.cn; Yongqi Zhang, yqzhang@uestc.edu.cn

In this study, we demonstrate our recent effort to advance this objective by fabricating NiFe alloy nanoparticles encapsulated within N-doped VG array on carbon cloth (NiFe@NVG/CC) via a rapid Joule heat (JH) process. When employed as a 3D electrode for OER, NiFe@NVG/CC exhibits robust catalytic activity, requiring only a 245 mV overpotential to achieve a current density (j) of 10 mA·cm^{-2} in a 1.0 M KOH electrolyte. Notably, this electrode showcases outstanding long-term electrochemical durability. Additionally, through density functional theory calculations (DFT), we elucidated the synergistic effect between NiFe and NVG, which enhances the adsorption capabilities of *OOH.

2 Experimental

2.1 Materials

Iron(III) acetylacetonate was bought from Shanghai Aladdin Biochemical Technology Co., Ltd., and urea and nickel(II) acetylacetonate were obtained from Shanghai Macklin Biochemical Co., Ltd. Ethanol was supplied by Sinopharm Chemical Reagent Co., Ltd. All chemicals were used as received without further purification. CC was obtained from CeTech Co., Ltd. Ultrapure water was used throughout the experiments.

2.2 Synthesis of VG/CC

VG/CC was synthesized using a custom-built plasma-enhanced chemical vapor deposition (PECVD) system. The PECVD was preheated to 500 °C, and CC substrate (20 mm × 50 mm) was positioned centrally. The system was evacuated to below 50 Pa before introducing a gas mixture of CH$_4$ (6 sccm), Ar (20 sccm), and H$_2$ (10 sccm). A 500 W radio frequency power source generated plasma for 8 min, with CH$_4$ as the carbon source for VG growth. The VG/CC was acquired subsequent to its cooling down to room temperature.

2.3 Synthesis of NiFe@NVG/CC

In synthesizing NiFe@NVG/CC, a precursor solution was first prepared by dissolving Ni-Fe metal precursor (mass ratio 7:3) at 10 mg·mL^{-1} and urea (20 mg·mL^{-1}, acting as a combustion promoter and N source) in ethanol. A VG/CC substrate (1.5 × 6 cm) was then immersed in this solution for 3 min to ensure complete impregnation. After air-drying, the substrate was placed in a homemade JH reaction chamber and subjected to a 10 A current for 0.2 s under vacuum to prevent oxidation. This process was repeated five times to yield NiFe@NVG/CC. Similar procedures were employed to fabricate NiFe@VG/CC, Ni@NVG/CC, Ni@VG/CC, Fe@NVG/CC, and Fe@VG/CC samples for comparative studies.

2.4 Characterization

The samples' physical and chemical properties were analyzed using X-ray diffraction (XRD, Rigaku Ultima IV), scanning electron microscopy (SEM, FEI Nova NanoSEM 450), transmission electron microscopy (TEM, FEI Tecnai G2 F20), X-ray photo electron spectroscopy (XPS, Axis Supra), and Raman spectroscopy (WITec-CRM200 Raman system with a laser wavelength of 532 nm). The contact angles of gas bubbles submerged in the electrolyte were tested using an OCA 50 AF (Dataphysics).

2.5 Electrochemical measurements

OER tests were performed on a CHI 660E workstation (Chenhua Instrument, China), with graphite and Hg/HgO electrodes as counter and reference electrodes, respectively. The working electrode was activated through 20 cyclic voltammetry (CV) cycles at 50 mV·s^{-1} between 1.0 and 1.7 V, and linear sweep voltammetry (LSV) scanning was conducted from 1.0 to 1.7 V at 5 mV·s^{-1}. Electrochemical impedance spectroscopy (EIS) measurements spanned between 10^5 and 10^{-2} Hz. Electrochemically active surface areas (ECSAs) were calculated from CV in the non-faradaic zone at 20–100 mV·s^{-1} scan rates. Catalyst durability was assessed using chronopotentiometry at 20–100 mA·cm^{-2} for 80 h. Potential scales were adjusted to reversible hydrogen electrode (RHE) using the Nernst equation ($E_{RHE} = E_{Hg/HgO} + 0.059 \times pH + 0.098$), and *iR* corrections were manually applied. All tests employed 1.0 M KOH electrolyte.

3 Results and discussion

The synthesis of NiFe@NVG/CC began with the growth of vertically aligned graphene arrays on CC via PECVD, followed by JH-driven growth of NiFe nanoparticles alloy on VG/CC, simultaneously achieving N doping (Fig. 1(a)). The XRD pattern of NiFe@NVG/CC, depicted in Fig. 1(b), exhibits characteristic peaks at 44.5° and 51.8°, which correspond respectively to the (111) and (200) crystallographic planes of FeNi$_3$ alloy (JCPDS No. 38-0419), respectively. Additionally, a broad peak at approximately 25°, indicative of carbon, is also observed [40, 41]. SEM images (Figs. 1(c) and 1(d) and Fig. S1 in the Electronic Supplementary Material (ESM)) illustrate the uniform distribution of NiFe nanoparticles across the 3D NVG, consistent with the morphology observed in NiFe@VG/CC synthesized without urea (Fig. S2 in the ESM). Further, TEM images (Figs. 1(e) and 1(f)) show numerous nanoparticles firmly anchored on the carbon sheets. The high-resolution TEM (HRTEM) image of a nanoparticle reveals a lattice spacing of 0.204 nm, indicative of the (111) plane of NiFe alloy. Elemental distribution analysis, conducted using high-angle annular dark-field scanning TEM (HAADF-STEM) (Fig. 1(h)) and corresponding elemental imaging, confirms the even dispersion of Ni, Fe, C, and N within NiFe@NVG.

The Raman spectrum of NiFe@NVG (Fig. 2(a)) displays two main peaks at 1332 and 1594 cm^{-1}, attributable to the D- and G-bands of carbon, respectively [42]. Bands at 477, 549, and 684 cm^{-1}, suggesting Ni–O and Fe–O vibrations, indicate partial oxidation of the FeNi alloy surface [43]. The XPS survey spectrum, as shown in Fig. 2(b), further confirms the presence of Ni, Fe, C, and N elements. Notably, the Ni 2p XPS spectra (Fig. 2(c)) display metallic Ni (Ni^0) peaks at 853.3/870.7 eV and Ni 2p$_{3/2}$ and Ni 2p$_{1/2}$ peaks at 856.1/874.4 eV in NiFe@NVG, accompanied by satellite peaks at 861.3 and 880.7 eV [32, 44, 45]. Furthermore, the Fe 2p high-resolution XPS spectra (Fig. 2(d)) show peaks at 706.6 and 718.5 eV for metallic Fe (Fe^0), with ionic Fe peaks at 710.6, 714.5, 724.3, and 726.4 eV, and satellite peaks at 714.4 and 732.5 eV [44, 46–48]. Additionally, the N 1s XPS spectrum (Fig. 2(e)) features peaks at 398.50, 399.53, 400.83, and 403.92 eV, aligning with pyridinic, pyrrolic, graphitic, and oxidized N, indicating successful N incorporation into NiFe@NVG [22, 31, 49]. The C 1s spectra (Fig. 2(f)) reveal peaks at 284.71, 285.56, and 287.52 eV, corresponding to C–C, C–N/C–O, and C=O [32, 34].

The OER activity of NiFe@NVG/CC was evaluated in a three-electrode cell employing a 1.0 M KOH electrolyte. This assessment included other Ni/Fe-based catalysts (NiFe@VG/CC, Fe@NVG/CC, Fe@VG/CC, Ni@NVG/CC, and Ni@VG/CC) for comparison purposes. And the XRD patterns, Raman spectra, and SEM images for these catalysts are presented in Figs. S3–S5 in the ESM. The polarization curves demonstrated NiFe@NVG/CC's superior performance, owing to its synergistic effect of Ni and Fe and a 3D NVG array (Fig. 3(a)). Remarkably, NiFe@NVG/CC
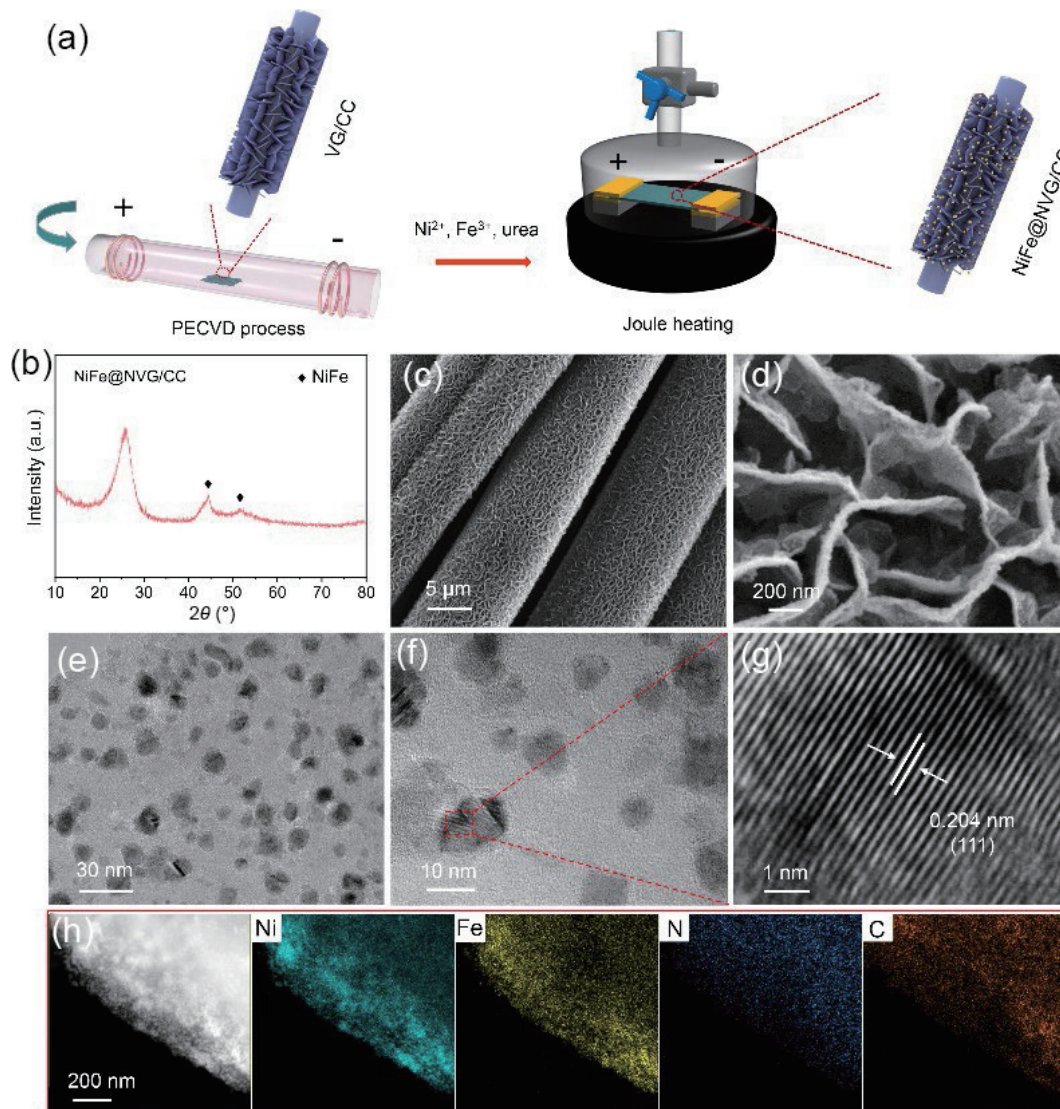
Figure 1 (a) Schematic of the synthesis process of NiFe@NVG/CC. (b) XRD pattern of NiFe@NVG/CC. (c) Low- and (d) high-magnification SEM images of NiFe@NVG/CC. (e) Low- and (f) high-magnification TEM and (g) HRTEM images of NiFe@NVG. (h) HAADF-STEM and its corresponding mapping images of NiFe@NVG.

achieved a j of 10 mA·cm^{-2} at a notably low overpotential of 245 mV, significantly outperforming NiFe@VG/CC (284 mV), Ni@NVG/CC (313 mV), Ni@VG/CC (335 mV), Fe@NVG/CC (377 mV), and Fe@VG/CC (351 mV), as shown in Fig. 3(b). Besides, NiFe@NVG/CC exhibits the smallest Tafel slope of 36.2 mV·dec^{-1} (vs. 86.9 mV·dec^{-1} for NiFe@VG/CC, vs. 82.7 mV·dec^{-1} for Ni@NVG/CC, vs. 58 mV·dec^{-1} for Ni@VG/CC, vs. 75 mV·dec^{-1} for Fe@NVG/CC, vs. 100 mV·dec^{-1} for Fe@VG/CC) (Fig. S6 in the ESM), proving the 3D NVG array's effectiveness in enhancing the OER catalytic kinetics of NiFe/CC. NiFe@NVG/CC, with its remarkably low overpotential and small Tafel slope, surpasses current NiFe-based alloys and most advanced OER electrocatalysts (Fig. 3(c) and Table S1 in the ESM). To evaluate ECSA, the electrochemical double-layer capacitance (C_{dl}) was measured. CV curves (Fig. S7 in the ESM) showed C_{dl} values (Fig. S8 in the ESM) for Ni-Fe-based samples: NiFe@NVG/CC (12.2 mF·cm^{-2}) demonstrated the highest ECSA, consistent with superior OER performance, surpassing NiFe@VG/CC, Ni@NVG/CC, Ni@VG/CC, Fe@NVG/CC, and Fe@VG/CC. And the Tafel slope of NiFe@NVG/CC significantly outperforms those of other Ni-, Fe-, or NiFe-based catalysts, underscoring its enhanced electrocatalytic efficiency (Fig. 3(d)). Furthermore, EIS measurements assessed charge transfer kinetics in synthesized catalysts. Nyquist plots (Fig. S9 in the ESM) across

samples indicated similar charge transfer processes and OER mechanisms. Variations in solution resistances among these catalysts in the same electrolyte are attributed to differing contact resistances between electrodes and electrolytes. Notably, NiFe@NVG/CC exhibits the lowest contact resistance. Its Nyquist plot shows the smallest semicircle diameter, which suggests that NiFe@NVG/CC has the lowest charge transfer resistance at the catalyst/electrolyte interface and the most rapid electron transfer rate during the OER. Besides, the stability of the catalyst is of critical importance for practical applications in water electrolysis. The multi-step chronopotentiometry curve of NiFe@NVG/CC catalysts was examined under various j, ranging from 20 to 100 mA·cm^{-2}, as depicted in Fig. 3(e). It illustrates a consistent capability to sustain a potential of 20 mA·cm^{-2} for 24 h. As the j was incrementally raised, there was a noticeable but modest decline in the potential activity. However, upon returning to 20 mA·cm^{-2}, the potential remained nearly constant within 24 h, and it verifies a slight impedance increase after continuous operation for 80 h at different j (Fig. S10 in the ESM), demonstrating robust electrolytic stability. Furthermore, NiFe@NVG/CC exhibited stable operation at 100 mA·cm^{-2} for 200 h in 1 M KOH (Fig. S11 in the ESM). Additionally, the XRD patterns (Fig. S12 in the ESM) and SEM image (Fig. S13 in the ESM) of NiFe@NVG/CC following an 80-h stability test affirmed
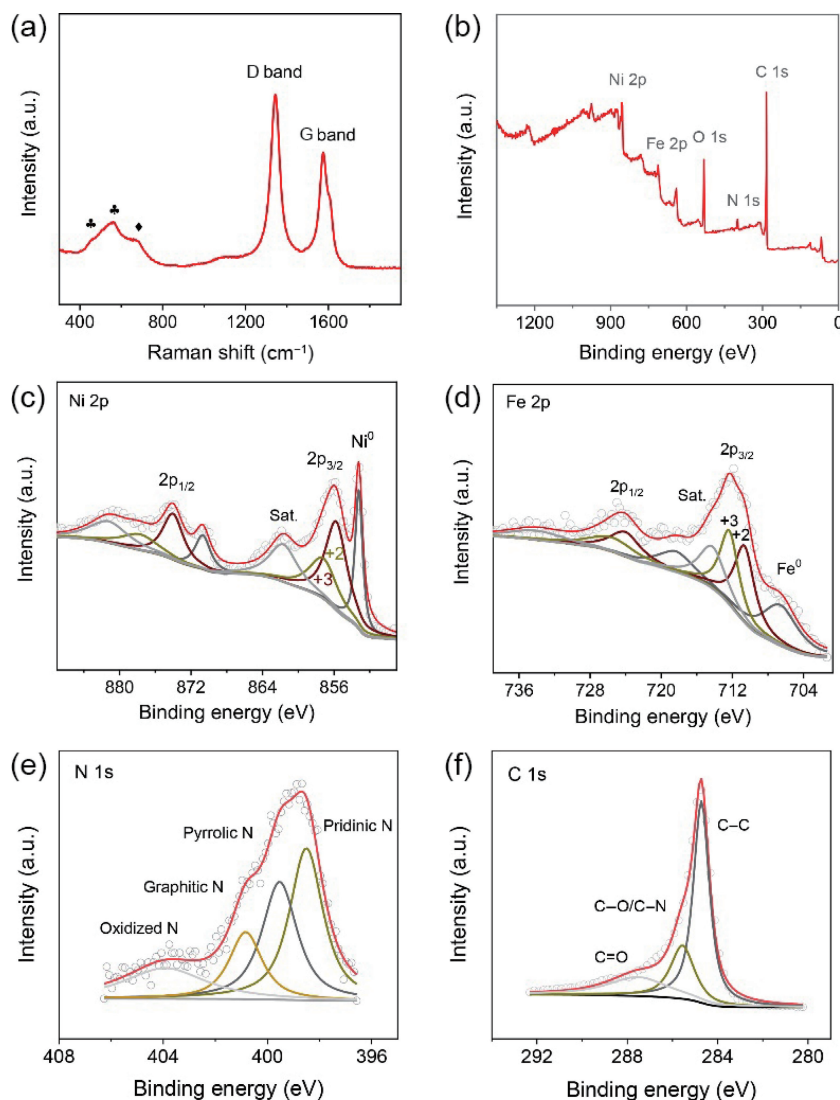
Figure 2 (a) Raman spectrum of NiFe@NVG. (b) XPS survey spectrum, and high resolution XPS spectra in the (c) Ni 2p and (d) Fe 2p, (e) N 1s, and (f) C 1s regions of NiFe@NVG.

the preservation of its crystalline structure and morphology. The TEM image of NiFe@NVG (Fig. S14(a) in the ESM) demonstrates the effective protection conferred by NVG, preventing significant coarsening or agglomeration of NiFe particles. Furthermore, the HRTEM image (Fig. S14(b) in the ESM) discloses a lattice fringe with a d-spacing of 0.256 nm, corresponding to the (100) crystal plane of NiFeOOH (JCPDS No. 14-0556), a feature emanating from the oxidized surface of the NiFe alloy during the OER test [29]. These observations are consistent with XPS depth profile results, which indicate an increase in Ni^{3+} and Fe^{3+} in NiFe@NVG (Fig. S15 in the ESM). Notably, NiFeOOH is identified as an active species for OER [25, 29].

DFT calculations were employed to elucidate the origin of the outstanding catalysis properties. The charge density difference diagram reveals the electron accumulation (yellow color) and depletion (cyan color) between NiFe and VG (NVG) layer (intermediate and the active site in the models). It was observed that enhanced electron transfer occurs on the surface of NiFe on NVG, suggesting increased electron distribution around the adsorbed intermediate, potentially boosting OER activity. It was further substantiated through an analysis of interfacial charge transfer, as elucidated by Bader charge calculations. Notably, the Bader charge alteration for NiFe@NVG was quantified at 1.85|e|, marginally exceeding that of NiFe@VG, which was measured at 1.81|e|, as depicted in Figs. 4(a) and 4(b). OER processes involve a

$4e^-$ transfer process with intermediates such as *OH, *O, and OOH, where the asterisk (*) represents active sites on the electrocatalyst surface [50]. Gibbs free energy calculations for these intermediates at $U = 0$ V on both NiFe@NVG and NiFe@VG (Fig. 4(c)) show that *OOH formation presents a significant energy barrier, identified as the rate-determining step for both catalysts. Notably, incorporating N into the VG layer of NiFe@NVG lowers this energy barrier, reducing it from 2.21 (NiFe@VG) to 2.18 eV (NiFe@NVG). A lower free energy correlates with reduced theoretical overpotential and enhanced catalytic activity [51]. These theoretical calculations align with our experimental findings, confirming that incorporating N species into the VG layer of NiFe@NVG enhances electrocatalytic activity by decreasing the reaction energy barrier during the conversion of *O to *OOH intermediates.

The outstanding OER performance of NiFe@NVG/CC can be attributed to several key factors: (1) 3D NVG array, notable for its abundant edges and expansive specific surface area, effectively anchors the NiFe alloy, impeding particles coarsening and thereby exposing numerous of active sites. (2) During the OER process, the *in-situ* formation of NiFeOOH acts as active site for the reaction. (3) Integrating N species into NiFe@NVG markedly boosts its electrocatalytic activity by reducing the energy barrier associated with the transformation of *O to *OOH intermediates. (4) The 3D array structure of NiFe@NVG/CC is beneficial to the
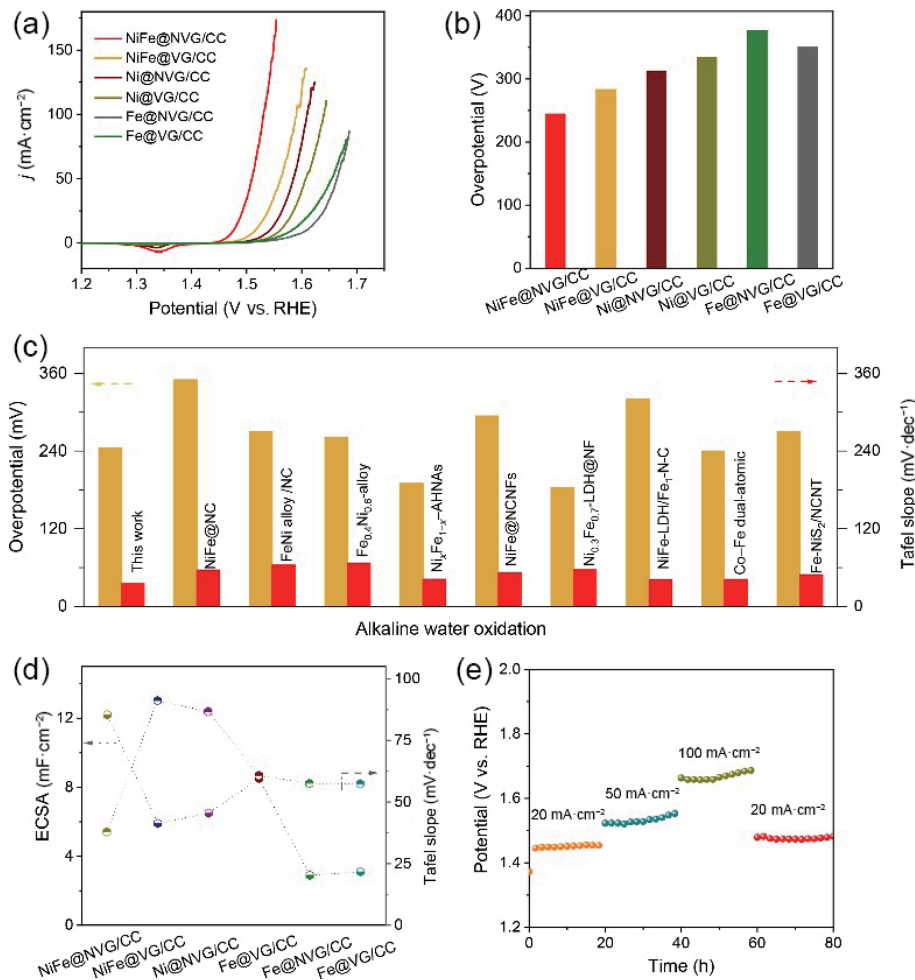
Figure 3 OER polarization curves (a) in 1 M KOH and (b) corresponding overpotential of Ni/Fe-based catalysts at a j of 10 mA·cm^{-2}. (c) Comparison of overpotentials at $j = 10$ mA·cm^{-2} and Tafel plots of NiFe@NVG/CC with other reported OER electrocatalysts. (d) Corresponding Tafel slopes and ECSA value of Ni/Fe-based catalysts. (e) Durability of NiFe@NVG/CC at various j.
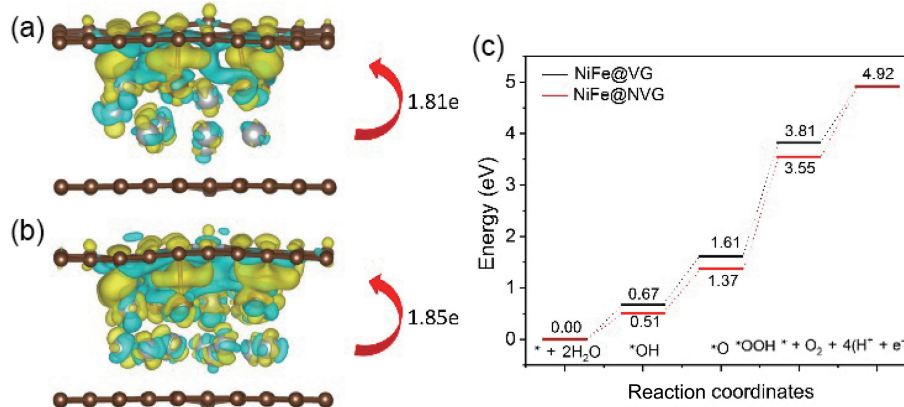

Figure 4 Charge density difference and Bader charge of (a) NiFe@VG and (b) NiFe@NVG (yellow region for charge accumulation, cyan region for charge depletion). (c) Gibbs free energy diagram of OER steps on models at $U = 0$ V.

mass transfer and bubble detachment, as evidenced by its exceptional surface wettability (Video ESM1).

4 Conclusions

In summary, Joule heating is proven as an effective strategy for rapid and facile fabrication of NiFe alloy nanoparticles encapsulated within a 3D NVG array on CC. Benefiting from the synergistic interplay of Ni, Fe, and NVG, the resulting NiFe@NVG/CC catalyst exhibits remarkable OER performance, including low overpotential, low Tafel slope, and excellent durability. This work not only offers a high-performance

electrocatalyst for alkaline water oxidation but would open new avenue to construct bis-transition-metal alloy@3D VG arrays for applications.

Electronic Supplementary Material: Supplementary material (SEM images, Table S1, and Video ESM1) is available in the online version of this article at https://doi.org/10.1007/s12274-024-6431-x.

References

[1] Seh, Z. W.; Kibsgaard, J.; Dickens, C. F.; Chorkendorff, I.; Nørskov, J. K.; Jaramillo, T. F. Combining theory and experiment in electrocatalysis: Insights into materials design. *Science* **2017**, *355*, eaad4998.

[2] Chu, S.; Majumdar, A. Opportunities and challenges for a sustainable energy future. *Nature* **2012**, *488*, 294–303.

[3] Liu, R.; Sun, M. Z.; Liu, X. J.; Lv, Z. H.; Yu, X. Y.; Wang, J. M.; Liu, Y. R.; Li, L. H.; Feng, X.; Yang, W. X. et al. Enhanced metal-support interactions boost the electrocatalytic water splitting of supported ruthenium nanoparticles on a Ni₃N/NiO heterojunction at industrial current density. *Angew. Chem., Int. Ed.* **2023**, *62*, e202312644.

[4] Zhou, J.; Wang, F. F.; Wang, H. Q.; Hu, S. X.; Zhou, W. J.; Liu, H. Ferrocene-induced switchable preparation of metal-nonmetal codoped tungsten nitride and carbide nanoarrays for electrocatalytic HER in alkaline and acid media. *Nano Res.* **2023**, *16*, 2085–2093.

[5] Zhang, K. X.; Liang, X.; Wang, L. N.; Sun, K.; Wang, Y. N.; Xie, Z. B.; Wu, Q. N.; Bai, X. Y.; Hamdy, M. S.; Chen, H. et al. Status and perspectives of key materials for PEM electrolyzer. *Nano Res. Energy* **2022**, *1*, e9120032.

[6] Jin, H. Y.; Yu, H. M.; Li, H. B.; Davey, K.; Song, T.; Paik, U.; Qiao, S. Z. MXene analogue: A 2D nitridene solid solution for high-rate hydrogen production. *Angew. Chem., Int. Ed.* **2022**, *61*, e202203850.

[7] Tian, C.; Liu, R.; Zhang, Y.; Yang, W. X.; Wang, B. Ru-doped functional porous materials for electrocatalytic water splitting. *Nano Res.*, in press, DOI: 10.1007/s12274-023-6003-5.

[8] Ouyang, L.; He, X.; Sun, Y. T.; Zhang, L. C.; Zhao, D. L.; Sun, S. J.; Luo, Y. S.; Zheng, D. D.; Asiri, A. M.; Liu, Q. et al. RuO₂ nanoparticle-decorated TiO₂ nanobelt array as a highly efficient electrocatalyst for the hydrogen evolution reaction at all pH values. *Inorg. Chem. Front.* **2022**, *9*, 6602–6607.

[9] Yang, W. X.; Zhang, W. Y.; Liu, R.; Lv, F.; Chao, Y. G.; Wang, Z. C.; Guo, S. J. Amorphous Ru nanoclusters onto Co-doped 1D carbon nanocages enables efficient hydrogen evolution catalysis. *Chin. J. Catal.* **2022**, *43*, 110–115.

[10] Wang, X. Y.; He, Y.; Han, X. P.; Zhao, J.; Li, L. L.; Zhang, J. F.; Zhong, C.; Deng, Y. D.; Hu, W. B. Engineering cobalt sulfide/oxide heterostructure with atomically mixed interfaces for synergistic electrocatalytic water splitting. *Nano Res.* **2022**, *15*, 1246–1253.

[11] Liang, J.; Li, Z. X.; He, X.; Luo, Y. S.; Zheng, D. D.; Wang, Y.; Li, T. S.; Ying, B. W.; Sun, S. J.; Cai, Z. W. et al. Electrocatalytic seawater splitting: Nice designs, advanced strategies, challenges and perspectives. *Mater. Today* **2023**, *69*, 193–235.

[12] Yang, W. X.; Wang, Z. C.; Zhang, W. Y.; Guo, S. J. Electronic-structure tuning of water-splitting nanocatalysts. *Trends Chem.* **2019**, *1*, 259–271.

[13] Jeon, S. S.; Kang, P. W.; Klingenhof, M.; Lee, H.; Dionigi, F.; Strasser, P. Active surface area and intrinsic catalytic oxygen evolution reactivity of NiFe LDH at reactive electrode potentials using capacitances. *ACS Catal.* **2023**, *13*, 1186–1196.

[14] Zhang, Y. Q.; Ouyang, B.; Xu, J.; Jia, G. C.; Chen, S.; Rawat, R. S.; Fan, H. J. Rapid synthesis of cobalt nitride nanowires: Highly efficient and low-cost catalysts for oxygen evolution. *Angew. Chem., Int. Ed.* **2016**, *55*, 8670–8674.

[15] Liu, X. J.; Liu, R.; Wang, J. M.; Liu, Y. R.; Li, L. H.; Yang, W. X.; Feng, X.; Wang, B. Synergizing high valence metal sites and amorphous/crystalline interfaces in electrochemical reconstructed CoFeOOH heterostructure enables efficient oxygen evolution reaction. *Nano Res.* **2022**, *15*, 8857–8864.

[16] Zhang, L. C.; Liang, J.; Yue, L. C.; Dong, K.; Li, J.; Zhao, D. L.; Li, Z. R.; Sun, S. J.; Luo, Y. S.; Liu, Q. et al. Benzoate anions-intercalated NiFe-layered double hydroxide nanosheet array with

[16] enhanced stability for electrochemical seawater oxidation. *Nano Res. Energy* **2022**, *1*, e9120028.

[17] Jin, H. Y.; Liu, X. Y.; An, P. F.; Tang, C.; Yu, H. M.; Zhang, Q. H.; Peng, H. J.; Gu, L.; Zheng, Y.; Song, T. et al. Dynamic rhenium dopant boosts ruthenium oxide for durable oxygen evolution. *Nat. Commun.* **2023**, *14*, 354.

[18] Wu, H.; Huang, Q. X.; Shi, Y. Y.; Chang, J. W.; Lu, S. Y. Electrocatalytic water splitting: Mechanism and electrocatalyst design. *Nano Res.* **2023**, *16*, 9142–9157.

[19] Sharma, L.; Katiyar, N. K.; Parui, A.; Das, R.; Kumar, R.; Tiwary, C. S.; Singh, A. K.; Halder, A.; Biswas K. Low-cost high entropy alloy (HEA) for high-efficiency oxygen evolution reaction (OER). *Nano Res.* **2022**, *15*, 4799–4806.

[20] Wang, L. G.; Su, H.; Zhang, Z.; Xin, J. J.; Liu, H.; Wang, X. G.; Yang, C. Y.; Liang, X.; Wang, S. W.; Liu, H. et al. Co-Co dinuclear active sites dispersed on zirconium-doped heterostructured Co₉S₈/Co₃O₄ for high-current-density and durable acidic oxygen evolution. *Angew. Chem., Int. Ed.* **2023**, *62*, e202314185.

[21] Zhai, Y. Y.; Ren, X. R.; Sun, Y.; Li, D.; Wang, B. L.; Liu, S. Z. Synergistic effect of multiple vacancies to induce lattice oxygen redox in NiFe-layered double hydroxide OER catalysts. *Appl. Catal. B Environ.* **2023**, *323*, 122091.

[22] Wei, P.; Sun, X. P.; Liang, Q. R.; Li, X. G.; He, Z. M.; Hu, X. S.; Zhang, J. X.; Wang, M. H.; Li, Q.; Yang, H. et al. Enhanced oxygen evolution reaction activity by encapsulating NiFe alloy nanoparticles in Nitrogen-doped carbon nanofibers. *ACS Appl. Mater. Interfaces* **2020**, *12*, 31503–31513.

[23] Wu, L. B.; Ning, M. H.; Xing, X. X.; Wang, Y.; Zhang, F. H.; Gao, G. H.; Song, S. W.; Wang, D. Z.; Yuan, C. Q.; Yu, L. et al. Boosting oxygen evolution reaction of (Fe,Ni)OOH via defect engineering for anion exchange membrane water electrolysis under industrial conditions. *Adv. Mater.* **2023**, *35*, 2306097.

[24] Wu, Q. N.; Wang, Y. N.; Zhang, K. X.; Xie, Z. B.; Sun, K.; An, W.; Liang, X.; Zou, X. X. Advances and status of anode catalysts for proton exchange membrane water electrolysis technology. *Mater. Chem. Front.* **2023**, *7*, 1025–1045.

[25] Liang, C. W.; Zou, P. C.; Nairan, A.; Zhang, Y. Q.; Liu, J. X.; Liu, K. W.; Hu, S. Y.; Kang, F. Y.; Fan, H. J.; Yang, C. Exceptional performance of hierarchical Ni-Fe oxyhydroxide@NiFe alloy nanowire array electrocatalysts for large current density water splitting. *Energy Environ. Sci.* **2020**, *13*, 86–95.

[26] Zhao, J.; Zhang, J. J.; Li, Z. Y.; Bu, X. H. Recent progress on NiFe-based electrocatalysts for the oxygen evolution reaction. *Small,* **2020**, *16*, 2003916.

[27] Gong, M.; Dai, H. J. A mini review of NiFe-based materials as highly active oxygen evolution reaction electrocatalysts. *Nano Res.* **2015**, *8*, 23–39.

[28] Kang, Q. L.; Lai, D. W.; Tang, W. Y.; Lu, Q. Y.; Gao, F. Intrinsic activity modulation and structural design of NiFe alloy catalysts for an efficient oxygen evolution reaction. *Chem. Sci.* **2021**, *12*, 3818–3835.

[29] Zhang, G. W.; Zeng, J. R.; Yin, J.; Zuo, C. Y.; Wen, P.; Chen, H. T.; Qiu, Y. J. Iron-facilitated surface reconstruction to *in-situ* generate nickel-iron oxyhydroxide on self-supported FeNi alloy fiber paper for efficient oxygen evolution reaction. *Appl. Catal. B Environ.* **2021**, *286*, 119902.

[30] Wang, A. Q.; Zhao, Z. L.; Hu, D.; Niu, J. F.; Zhang, M.; Yan, K.; Lu, G. Tuning the oxygen evolution reaction on a nickel-iron alloy via active straining. *Nanoscale,* **2019**, *11*, 426–430.

[31] Feng, Y.; Yu, X. Y.; Paik, U. N-doped graphene layers encapsulated NiFe alloy nanoparticles derived from MOFs with superior electrochemical performance for oxygen evolution reaction. *Sci. Rep.* **2016**, *6*, 34004.

[32] Gong, Z. C.; Liu, R.; Gong, H. S.; Ye, G. L.; Liu, J. J.; Dong, J. C.; Liao, J. W.; Yan, M. M.; Liu, J. B.; Huang, K. et al. Constructing a graphene-encapsulated amorphous/crystalline heterophase NiFe alloy by microwave thermal shock for boosting the oxygen evolution reaction. *ACS Catal.* **2021**, *11*, 12284–12292.

[33] Feng, Y. Y.; Zhang, H. J.; Fang, L.; Mu, Y. P.; Wang, Y. Uniquely monodispersing NiFe alloyed nanoparticles in three-dimensional strongly linked sandwiched graphitized carbon sheets for high-

efficiency oxygen evolution reaction. *ACS Catal.* **2016**, *6*, 4477–4485.

[34] Zhang, Z. P.; Qin, Y. S.; Dou, M. L.; Ji, J.; Wang, F. One-step conversion from Ni/Fe polyphthalocyanine to N-doped carbon supported Ni-Fe nanoparticles for highly efficient water splitting. *Nano Energy* **2016**, *30*, 426–433.

[35] Zhang, L.; Hu, J. S.; Huang, X. H.; Song, J.; Lu, S. Y. Particle-in-box nanostructured materials created via spatially confined pyrolysis as high performance bifunctional catalysts for electrochemical overall water splitting. *Nano Energy* **2018**, *48*, 489–499.

[36] Zhang, Z. Y.; Lee, C. S.; Zhang, W. J. Vertically aligned graphene nanosheet arrays: Synthesis, properties and applications in electrochemical energy conversion and storage. *Adv. Energy Mater.* **2017**, *7*, 1700678.

[37] Mu, Y. B.; Han, M. S.; Wu, B. K.; Wang, Y. M.; Li, Z. W.; Li, J. X.; Li, Z.; Wang, S.; Wan, J. Y.; Zeng, L. Nitrogen, oxygen-codoped vertical graphene arrays coated 3D flexible carbon nanofibers with high silicon content as an ultrastable anode for superior lithium storage. *Adv. Sci.* **2022**, *9*, 2104685.

[38] Wang, Y. L.; Shi, R.; Shang, L.; Peng, L. S.; Chu, D. W.; Han, Z. J.; Waterhouse, G. I. N.; Zhang, R.; Zhang, T. R. Vertical graphene array for efficient electrocatalytic reduction of oxygen to hydrogen peroxide. *Nano Energy* **2022**, *96*, 107046.

[39] Fang, R. P.; Han, Z. J.; Li, J. B.; Yu, Z. C.; Pan, J.; Cheong, S.; Tilley, R. D.; Trujillo, F.; Wang, D. W. Rationalized design of hyperbranched trans-scale graphene arrays for enduring high-energy lithium metal batteries. *Sci. Adv.* **2022**, *8*, eadc9961.

[40] He, X.; Li, X. H.; Fan, X. Y.; Li, J.; Zhao, D. L.; Zhang, L. C.; Sun, S. J.; Luo, Y. S.; Zheng, D. D.; Xie, L. S. et al. Ambient electroreduction of nitrite to ammonia over Ni nanoparticle supported on molasses-derived carbon sheets. *ACS Appl. Nano Mater.* **2022**, *5*, 14246–14250.

[41] Ding, P.; Song, H. Q.; Chang, J. W.; Lu, S. Y. N-doped carbon dots coupled NiFe-LDH hybrids for robust electrocatalytic alkaline water and seawater oxidation. *Nano Res.* **2022**, *15*, 7063–7070.

[42] Ha, Y.; Shi, L. X.; Yan, X. X.; Chen, Z. L.; Li, Y. P.; Xu, W.; Wu, R. B. Multifunctional electrocatalysis on a porous N-doped NiCo₂O₄@C nanonetwork. *ACS Appl. Mater. Interfaces* **2019**, *11*, 45546–45553.

[43] Xie, C.; Wang, Y. Y.; Hu, K.; Tao, L.; Huang, X. B.; Huo, J.; Wang, S. Y. *In situ* confined synthesis of molybdenum oxide decorated nickel-iron alloy nanosheets from MoO_4^{2-} intercalated layered double hydroxides for the oxygen evolution reaction. *J. Mater. Chem. A* **2017**, *5*, 87–91.

[44] Chen, Y. H.; Peng, J.; Duan, W. T.; He, G. Q.; Tang, Z. H. NiFe alloyed nanoparticles encapsulated in nitrogen doped carbon nanotubes for bifunctional electrocatalysis toward rechargeable Zn-air batteries. *ChemCatChem* **2019**, *11*, 5994–6001.

[45] He, X.; Hu, L.; Xie, L. S.; Li, Z. R.; Chen, J.; Li, X. H.; Li, J.; Zhang, L. C.; Fang, X. D.; Zheng, D. D. et al. Ambient ammonia synthesis via nitrite electroreduction over NiS₂ nanoparticles-decorated TiO₂ nanoribbon array. *J. Colloid Interface Sci.* **2023**, *634*, 86–92.

[46] Han, Q. L.; Luo, Y. H.; Li, J. D.; Du, X. H.; Sun, S. J.; Wang, Y. J.; Liu, G. H.; Chen, Z. W. Efficient NiFe-based oxygen evolution electrocatalysts and origin of their distinct activity. *Appl. Catal. B Environ.* **2022**, *304*, 120937.

[47] He, X.; Li, J.; Li, R. Z.; Zhao, D. L.; Zhang, L. C.; Ji, X. C.; Fan, X. Y.; Chen, J.; Wang, Y.; Luo, Y. S. et al. Ambient ammonia synthesis via nitrate electroreduction in neutral media on Fe₃O₄ nanoparticles-decorated TiO₂ nanoribbon array. *Inorg. Chem.* **2023**, *62*, 25–29.

[48] Liu, B.; Yuan, B. W.; Wang, C.; You, S. J.; Liu, J.; Meng, X.; Xu, X. Q.; Cai, Z.; Xie, J. H.; Zou, J. L. Highly-dispersed NiFe alloys *in-situ* anchored on outer surface of Co, N co-doped carbon nanotubes with enhanced stability for oxygen electrocatalysis. *J. Colloid Interface Sci.* **2023**, *635*, 208–220.

[49] Huang, L.; Guan, T. X.; Su, H.; Zhong, Y.; Cao, F.; Zhang, Y. Q.; Xia, X. H.; Wang, X. L.; Bao, N. Z.; Tu, J. P. Synergistic interfacial bonding in reduced graphene oxide fiber cathodes containing polypyrrole@sulfur nanospheres for flexible energy storage. *Angew. Chem.* **2022**, *134*, e202212151.

[50] Wu, H.; Wang, Z. C.; Li, Z. X.; Ma, Y. J.; Ding, F.; Li, F. Q.; Bian, H. F.; Zhai, Q. X.; Ren, Y. L.; Shi, Y. X. et al. Medium-entropy metal selenides nanoparticles with optimized electronic structure as high-performance bifunctional electrocatalysts for overall water splitting. *Adv. Energy Mater.* **2023**, *13*, 2300837.

[51] Liu, P.; Rodriguez, J. A. Catalysts for hydrogen evolution from the [NiFe] hydrogenase to the Ni₂P(001) surface: The importance of ensemble effect. *J. Am. Chem. Soc.* **2005**, *127*, 14871–14878.